HHS Public Access

Author manuscript

J Neurosci Methods. Author manuscript; available in PMC 2022 August 31.

Published in final edited form as:

J Neurosci Methods. 2019 February 01; 313: 68–76. doi:10.1016/j.jneumeth.2018.12.008.

Seeing the long tail: A novel green fluorescent protein, SiriusGFP, for ultra long timelapse imaging

Sheng Zhong[a,e], **Felix Rivera-Molina**[b], **Alberto Rivetta**[d], **Derek Toomre**[b], **Joseph Santos-Sacchi**[a,c,d], **Dhasakumar Navaratnam**[a,c,e,*]

[a]Dept. of Surgery (Otolaryngology), Yale University School of Medicine, New Haven, CT, 06511, United States

[b]Dept. of Cell Biology, United States

[c]Dept. of Neuroscience, United States

[d]Dept. of Cellular and Molecular Physiology, United States

[e]Dept. of Neurology, United States

Abstract

Background: Fluorescent proteins (FPs) have widespread uses in cell biology. However, the practical applications of FPs are significantly limited due to their rapid photobleaching and misfolding when fused to target proteins.

New Method: Using a combination of novel and known mutations to eGFP, we developed a well folded and very photostable variant, SiriusGFP.

Results: The fluorescence spectrum indicated that the excitation and emission peaks of SiriusGFP were red-shifted by 16 and 8 nm, respectively. Co-operative effects of two key mutations, S147R and S205 V, contribute to its photostability. SiriusGFP tagged to the mitochondrial outer membrane protein Omp25 showed sustained fluorescence during continuous 3D-scanning confocal imaging (4D confocal) compared to eGFP-tagged Omp25. Furthermore, with super-resolution structured illumination microscopy (SIM) we demonstrate marked improvements in image quality and resolution (130 nm in XY axis, and 310 nm in Z axis), as well as, decreased artifacts due to photobleaching.

Comparison with Existing Method(s): Compared to eGFP. SiriusGFP shows a 2-fold increase in photostability in vitro, and folds well when fused to the N- and C- termini of cytoplasmic and membrane proteins. While its quantum yield is ˜3 fold lower than eGFP, its decreased brightness was more than compensated by its increasedphotostability in different experimental paradigms allowing practical experimentation without dynamic adjustment of light intensity or fluorescence sampling times.

*Corresponding author at: Dept of Neurology, Yale School of Medicine, New Haven, Connecticut, 06511, United States. dhasakumar.navaratnam@yale.edu (D. Navaratnam).

Appendix A. Supplementary data

Supplementary material related to this article can be found, in the online version, at doi:https://doi.org/10.1016/j.jneumeth.2018.12.008.

Conclusions: We have developed a variant of eGFP, SiriusGFP, that shows over a two fold increase in photostability with utility in methods requiring sustained or high intensity excitation as in 4D confocal or SIM imaging.

Keywords

SiriusGFP; GFP; Fluorescence; 4D confocal; Structured Illumination Microscopy; Photostable

1. Introduction

Fluorescent proteins (FPs) are widely used in cellular imaging for recording subcellular events and detailed dynamic processes, including *in vivo* imaging. In the nervous system, fluorescent proteins have been used for temporospatial migration of individual cells and to ascertain numerous physiological phenomena including changes in membrane potential and Ca^{2+} and Cl^{-} levels (Baker, Mutoh et al. 2008; Chen, Wardill et al. 2013; Zhong, Navaratnam et al. 2014). Compared to chemical dyes, genetically encoded FPs have many benefits including 1) precise targeting with fusion proteins 2) avoidance of chemical loading/labelling with consequent cell toxicity and dye leakage/delocalization. Perhaps the most distinguishing advantage of FPs is genetic labeling that allows potential development of cell-lines and transgenic animals with the gene-editing tool CRISPR/Cas9 and tissue-specific gene expression.

Recently, the expansion in 3D time-lapse (4D) confocal imaging of cells during development and super-resolution microscopic technologies have required brighter, photostable fluorophores for imaging. Photobleaching is one of the major problems for FPs, which limits their applications in biological investigation. Reduced light emission due to photobleaching can be compensated by increases in excitation light intensity and exposure time. These two compensatory mechanisms also compensatory mechanisms are not possible for the fast imaging times used in modern fluorescence imaging techniques. For confocal microscopy and almost all superresolution microscopy methods, photostability is as important a factor as brightness for imaging quality. For super-resolution structured illumination microscopy (SIM), in particular, the requirement of at least 15 frames (3 angles and 5 phases per angle) to generate a single image makes it more sensitive to photobleaching than conventional confocal microscopy (Rego and Shao, 2015; Hong, Wilton et al. 2017).

The green fluorescent protein (GFP) and its variants derived from jellyfish *Aequorea victoria* are the most extensively used FPs. eGFP is the most widely used FP, but has significant drawbacks in biological applications. The chromophore in GFPs, *para*-hydroxybenzylidene-imidazolinone (*p*-HBDI), is formed by sequential autocatalytic cyclization and dehydration/oxidation, after initial folding of the polypeptide chain into a β-barrel conformation. For *p*-HBDI, the *Z-E* isomerization on the exocyclic double bond is the major internal conversion pathway, the non-fluorescent alternative pathway of energy dissipation of the excited fluorophore. The fluorescence quantum yield (φ_f) of *p*-HBDI (without the surrounding β-barrel) is < 0.001 in gas phase (Huang, Cheng et al. 2013), and even lower (˜ 0.0001) in solvents, while the quantum yield (φ_{ZE}) of *Z-E* isomerization is ˜0.5 (Yang, Huang et al. 2008; Chatterjee, Mandal et al. 2015). The β-barrel scaffold of GFP provides hydrophobic

isolation and a rigidly constrained environment for the chromophore, functioning as a protective nest for efficient production of fluorescence. As a result, the quantum yield of GFP can reach up to 0.77 (as reference, 0.80 for frozen *p*-HBDI at 77 K, where the internal conversion pathway is almost eliminated) (Niwa, Inouye et al. 1996; Nielsen, Lapierre et al. 2001).

How irreversible photobleaching of the chromophore in FPs occurs is not clear, although oxygen concentration dependence on photobleaching has been confirmed in many GFP-like FPs. The destruction of chromophores in chemical dyes is preceded by ROS formation from redox reactions with the excited chromophore. The formation of ROS is, in turn, strongly dependent on the local redox environment. The damage to the chromophore in GFP is likely caused by endogenous and exogenous singlet oxygen. For wtGFP or eGFP, self-generated endogenous singlet oxygen ($^1O_2$) occurs when exposed to illumination (Greenbaum, Rothmann et al. 2000; Jimenez-Banzo, Nonell et al. 2008; Bogdanov, Bogdanova et al. 2009). The formation of superoxide was postulated to be the gateway initiating a series of chemical reactions leading to the destruction of the chromophore (Chatterjee, Mandal et al. 2015). Furthermore, solvated electrons produced from solvent radiolysis outside the β-barrel can migrate to the chromophore cavity through a water tunnel near residue His148. Therefore, it is possible to reduce photosensitized $^1O_2$ by limiting the accessibility of molecular oxygen to the chromophore; a tighter β-can or an allosteric block are two potential ways.

Based on the knowledge of fluorophore photochemistry, we developed a series of eGFP derivatives to increase photostability that can tolerate higher intensity illumination and longer exposure. The best variant, SiriusGFP, contains several folding mutations and two key mutations, S147R and S205 V, both of which contribute to significant improvement in photostability over eGFP. Although SiriusGFP has reduced brightness compared to eGFP, it is more than compensated for by an increase in photostability. Practically, this allowed for improved 4D confocal imaging as it eliminated dynamic adjusting of exposure time. Furthermore, SIM images with SiriusGFP show resolution improvement, especially in the Z axis. The optical properties were determined with purified protein of SiriusGFP, and compared to eGFP. The photobleaching mechanism of SiriusGFP was determined to be oxygen-dependent under oxygen-depletion in both high and low intensity illumination. This contrasts with eGFP that shows different mechanisms and sensitivities to oxygen with high and low laser power. Our new green FP, SiriusGFP, provides improved capabilities for superresolution and time-lapse microscopy.

2. Methods

2.1. Gene construct and mutations & cell culture

Mutagenesis was performed using the Quick Change method adapted from Stratagene QC protocol. Mutations were verified by DNA sequencing the entire gene. We used EGFP-N1 as the backbone vector. HEK-293 and HeLa cells were cultured in Dulbecco's modified Eagle's medium (DMEM, high glucose) containing 50 U/ml penicillin and streptomycin (1%), 10% fetal bovine serum (FBS) at 37 °C in a CO_2incubator (5%).

The sequences of SiriusGFP and the intermediates of SG205 and SG147 are as followed.

SG205: eGFP-**S205V**/A206K

SG147: eGFP-**S147R**/A206K

SiriusGFP: eGFP-S30R/Y39 N/F99S/N105 T/**S147R**/M153 T/V163 A/**S205V**/A206K

2.2. Fluorescent protein extraction from cell lysis

Cultured HEK-293 cells were grown in 10 cm dishes and transiently transfected with eGFP and SiriusGFP plasmid, respectively. After 48 h of incubation, the cells were scraped with a plastic scraper after a brief rinse in DPBS. Cells were resuspended in 200 ul of EBC buffer (50 mM Tris, 120 mM NaCl, 0.5% NP40, pH 7.5) containing Protease Inhibitor cocktail (ThermoFisher, PI-88665), vortexed at 4 °C for 15 min to lyse the cells, and then centrifuged at 14,000 rpm for 20 min (4 °C). The supernatant containing solubilized fluorescent proteins was aspirated and used for further experimentation.

2.3. Expression and purification of eGFP and SiriusGFP

SiriusGFP and eGFP proteins were expressed in *E. coli* and purified by immobilized metal ion affinity chromatography. eGFP and SiriusGFP genes were subcloned in the pQE-80 l vector (Qiagen) using BamHI and HindIII restriction sites. The vector is designed to provide a six-histidine tag on the N-terminus of the expressed EGFP and SiriusGFP for affinity purification. The complete tag sequence fused to the actual eGFP and SiriusGFP proteins was MRGSHHHHHHGS. The constructs were transformed in *E. coli* BL21(DE3), spread on LB plates containing 100 μg/ml ampicillin (LBA), and incubated overnight at 37 °C A single colony from each construct was inoculated in 50 ml LBA and incubated for 16 h at 37 °C without shaking. The resulting seed culture was added to 500 ml LBA in a 2-liter baffled Erlenmeyer flask, and incubated at 37 °C in an orbital shaker (150 rpm) until OD_{600} reached 0.6–0.7. The flasks were quickly cooled under running tap water and the cultures injected with 0.5 mM isopropyl β-D-1-thiogalactopyranoside (IPTG) to induce protein expression. The cultures were incubated with shaking (150 rpm) for a further 22 h at 15 °C until it reached a final density OD_{600} ~5. Cells were pelleted by centrifugation (4000 *g*/10 min) and the pellets resuspended in 40 ml Buffer A: 50 mM NaH_2PO_4 (titrated to pH 8 with NaOH), 300 mM NaCl. Temperature was kept at 4C throughout cell lysis and purification steps. After addition of protease inhibitor cocktail (10 μg/ml each of aprotinin, leupeptin, pepstatin, chymostatin) and 10 mM imidazole, the cell slurry was sonicated using a Brenson digital sonifier (6 cycles of 30 s each, at 67% amplitude). Cell lysates were centrifuged for 40 min at 15,000 *g*, and the supernatant added to a 1 ml bed volume of Ni-NTA agarose resin (Qiagen) and gently nutated for 1 h. The resin was loaded on a column and sequentially washed with 10 ml Buffer A plus 10 mM imidazole, and 10 ml Buffer A plus 20 mM imidazole. Fluorescent proteins were eluted using Buffer A containing 250 mM imidazole and dialyzed against 1 L of 20 mM Tris (titrated to pH 7.5 with HCl) and 150 mM NaCl. Protein concentration was measured with the Bradford method (Bradford, 1976; Thermoscientific/Pierce Coomassie Protein Assay Kit), using bovine serum albumin as a calibration standard. Both eGFP and SiriusGFP proteins ran as a single band at ~25

kDa molecular weight on SDS-PAGE gel (Bio-Rad Mini-Protean TGX gel, 4–15%). Typical protein yields for both eGFP and SiriusGFP were about 40 mg per liter of culture.

2.4. Optical properties

The absorbance spectroscopy of purified FPs was performed in 150 mM NaCl, 20 mM Tris, pH 7.5 with an Agilent 8453 UV–vis spectroscope. The fluorescence spectra of purified FPs was obtained in the same buffer in a FluoroMax-3 (Jobin Yvon Horiba). The quantum yields were calculated from the spectral readout.

2.5. Wide-filed photobleaching on live cells

The cultured cells were grown on glass coverslips (No.1, 0.13–0.16 mm thick, 15 mm round, Warner Instr., USA). Transient transfection with the plasmid of interest was performed using lipofectamine-2000 (Invitrogen, Life technologies). After transfection, the coverslips were mounted on a quick change chamber and platform (RC-42LP and QE-1, Warner Instr., USA). Fluorescence images were acquired using an oil-immersion objective (N.A. = 1.30, Plan Fluor 100× Objective, Nikon, Japan) with a Nikon *Eclipse Ti* equipped with a 200 W metal-halide lamp (Lumen200, Prior Scientific, USA) as the fluorescence illumination source. Shutter and filter wheel (Lambda10–3 optical filter changer with smart shutter, Sutter Instr., USA) were connected between the microscope and the illumination source, in which Semrock ET430/24x-32 was used as the excitation filter for CFP, Semrock ET500/20x-32 as the excitation filter for YFP and Chroma HQ520LP as the emission filter. A 14-bit back-illuminated EMCCD camera system (128 × 128 pixels, 24 μm array, Andor iXon^{EM}+ DU-860E, USA) was used to record the fluorescence images under 430 or 500 nm excitation. All peripheral hardware control, image acquisition and image processing were achieved and/or synchronized on a PC computer via a 16-bit/1-MHz USB Data Acquisition System (Personal Daq/3000 Series, IOtech, USA) by using customized software (jClamp & FastLook, SciSoft, USA; www.SciSoftCo.com). Photobleaching data and fluorescence images were achieved with our ratiometric imaging system controlled by jClamp & FastLook. Photobleaching efficiency at a wavelength of 430 nm is higher than at 500 nm, although the absorption at 430 nm is much lower than 500 nm. Because of this enhanced bleaching capability and to optimize our identification of photostable products, we bleached GFP variants at 430 nm (approximately 1 mW with the 100X objective). Stable optical power at the utilized wavelengths was confirmed using an analog optical power meter (ThorLabs PM30–130, w/S130 A Slim Sensor). The 430 nm filter was used for 60 ms at the beginning of each episode and then the filter changed to 500 nm, an image acquired, and then the filter changed back to 430 nm for bleaching for a further 2 s. This procedure was performed reiteratively for 400 episodes. Filter changes required 100 ms. There is a 200 ms interval time between two successive episodes, and the excitation filter remained at 430 nm between successive episodes. The photobleaching curves were measured in GFP variants expressed in the cytosol of HEK-293 cells. The average fluorescence intensity of regions of interest (ROI) was measured, and the background fluorescence was subtracted using FastLook and ImageJ. Data were analyzed with Matlab, Origin 2016 and SigmaPlot 10.0.

2.6. Confocal photobleaching on live cells

The photobleaching of live Hela cells was performed on a Zeiss LSM 710 duo confocal scanning microscope with an OPSS laser at 489 nm (100 mW at maximum power). Hela cells were grown on 35 mm glass-bottom culture petri dishes (P35GC-1.0–14-C, MatTek, USA), and transfected with eGFP/SG205/SG147/SiriusGFP plasmids using Lipofectamine 2000 (Invitrogen, USA) followed by 24 h incubation at 37 °C. Before imaging, culture media in petri dishes was changed to a neutral buffer of 0.2 mM NaCl, 100 mM sodium Malate, 300 mOsm, pH 7.20 after a rinse with PBS. All photobleaching data were fit by a single exponential decay function, $Y = Y_0 + Ae^{-x/t}$, where Y_0 is the constant offset representing the residual fluorescence after photobleaching reaching a steady state (R^2 ranged from 0.97–0.99). The laser power was measured with an analog optical power meter (ThorLabs PM30–130, w/S130 A Slim Sensor).

2.7. Oxygen-depletion photobleaching

The photobleaching of PFA-fixed Hela cells are performed in the same Zeiss LSM 710 duo confocal microscope. The oxygen-depletion buffer containing COT was prepared as previously described (Olivier, Keller et al. 2013). Mercaptoethylamine (**MEA**, Sigma-Aldrich 30,070) was dissolved in deionized water as 1 M stock solution, then adjusted to ˜pH 8 by glacial acetic acid (Avantor Performance Materials). The stock solution was stored at 4 °C and used within a week. β-mercaptoethanol (**BME**, Sigma M3148) was used without dilution as a 14.3 M solution. Cyclooctatetraene (**COT**, Sigma-Aldrich 138,924) was diluted in DMSO as 200 mM stock solution and stored at 4 °C. Protocatechuic acid (**PCA**, Sigma-Aldrich 37,580) was dissolved in deionized water as 100 mM stock solution, then adjusted to pH 9 with KOH aq. The stock solution was stored at 4 °C and used within a month. Protocatechuate 3,4-dioxygenase from *Pseudomonas* sp. (**PCD**, Sigma-Aldrich P8279) was dissolved in 100 mM Tris−HCl (pH 8) containing 50 mM KCl, 1 mM EDTA and 50% glycerol as 5 μM stock solution, and stored at −20 °C.

Before oxygen-depletion treatment and confocal imaging, HELA cells transfected with eGFP-Omp25 or SiriusGFP-Omp25 were fixed with 4% PFA for 10 min, and the coverslips rinsed with PBS 3 times. Cells were treated with 0.2% Triton X-100 in PBS for 15 min to permeabilize cell membranes. Coverslips were rinsed with PBS 3 times. Confocal imaging was performed with a Zeiss LSM710 Duo confocal scanning microscope in freshly made oxygen-depletion solution of 10 mM PBS-Tris (pH 7.5) containing 10% (w/v) glucose, 10 mM MEA, 50 mM BME, 2 mM COT, 2.5 mM PCA and 50 nM PCD. This oxygen-depletion solution was abbreviated as pcaPCD in the Fig. 2. Controls were in 10 mM PBS-Tris buffer containing 10% glucose. The maximum optical power of the OPSS laser is 100 mW, and 5% (low intensity) and 50% (high intensity) were the percentage of laser power used for photobleaching.

2.8. Photobleaching on purified protein embedded in gel

Photobleaching rates on purified proteins of GFPs embedded in polyacrylamide gel were measured by Zeiss LSM710 laser-scanning confocal microscopy, following a previously described protocol (Cranfill, Sell et al. 2016). This experiment was designed to produce a homogenous population of immobilized protein of known concentration which was

photobleached. Briefly, 20% polyacrylamide-1uM FP solution was polymerized by addition of ammonium persulfate and TEMED. The 20% polyacrylamide-1uM FP solution was then injected into a space between a coverslip and glass slide. After polymerization of the acrylamide the outside edges of the coverslip were sealed with Cytoseal to prevent dehydration around the edges. The slides were maintained in the dark at 4 °C overnight before photobleaching and imaging.

2.9. Confocal 4D imaging

Confocal 4D imaging of live HeLa cells transfected with eGFP-Omp25 and SiriusGFP-Omp25, respectively. We used a Yokogawa CSU-X1 spinning disc confocal microscope for image acquisition. The 3D confocal Z-stack scanning was done continuously to maximize photobleaching.

2.10. Structured illumination microscopy (SIM)

HEK-293 or Hela cells were transfected with eGFP-Omp25 or SiriusGFP-Omp25, and incubated at 37 °C in a CO_2incubator (5%). The targeting protein embedded in the outer membrane of mitochondria in HEK-293 or Hela cells. Before imaging, cells were fixed with 4% PFA and then rinsed with PBS buffer. Structured Illumination Microscopy (SIM, DeltaVision-OMX, Applied Precision, GE life) was performed in PBS. The XY and Z resolution were measured with the lines perpendicularly across individual mitochondrial membranes at XY and XZ/YZ axes, respectively. Gaussian fitting of the readout traces gives full width at half maximum (FWHM) of each peak. Averages of over 100 peaks in SIM images were measured to ascertain the resolution of the imaging technique.

3. Results

3.1. Optical properties of SiriusGFP

Mutations of F99S/M153 T/V163 A in Cycle3 GFP help folding and maturation by avoiding aggregation traps (Fukuda, Arai et al. 2000), and S30R/Y39 N/N105 T help fast folding in super-folder GFP/YFP (Pedelacq, Cabantous et al. 2006; Andrews, Schoenfish et al. 2007; Ottmann, Weyand et al. 2009). A206 K mutation makes GFP fully monomeric even at high concentrations (Zacharias, Violin et al. 2002), which eliminates the multimerization/aggregation of GFP in fusion proteins.

Upon illumination, the neutral chromophore HBDI of wtGFP is excited and converted to the anion excited state, via excited state proton transfer (ESPT), in the picosecond timescale. It was reported that the mutant S205 V of wtGFP has ESPT 30 times slower than in wtGFP through an alternative proton wire via T203 to E222 (Shu, Leiderman et al. 2007; Fang, Frontiera et al. 2009). And ESPT in S205 A is 15 times slower than wtGFP (Erez, Gepshtein et al. 2011; Wineman-Fisher, Simkovitch et al. 2014). Our previous work on chloride-sensitive YFP also indicated that S205 V in eYFP substantially increased the photostability (Zhong, Navaratnam et al. 2014). However, the double mutant of eGFP-T203 V/S205 V is still fluorescent when excited at 488 nm (data not shown), confirming that the majority of its chromophore stays in the anionic state, and ESPT is not necessary for fluorescence emission in eGFP.

Currently, Emerald GFP is the most photostable GFP variant, but exhibits a very fast initial fluorescence decay to about 50% before reaching a photostable state (Tsien, 1998; Cubitt, Woollenweber et al. 1999). This fast decay component makes Emerald less ideal for long term imaging or superresolution imaging. The key mutation in Emerald GFP is N149 K. We tested this mutation based on SG205 (S205 V/A206 K) by generating several mutants including N149 K, S147 H/N149 K, and Y145 F/S147 P/N149 K, respectively. However, all of these mutants still showed the fast initial decay (data not shown).

Based on the photobleaching results of the intermediate mutant SG147 (S147R/A206 K), we generated a mutation S147R that also increased both fluorescence lifetime (Tau) and residual fluorescence after photobleaching (Y_0). The increased Tau and Y_0 may be attributed to the protective effect of charge repulsion of positive ions (including protons) by the bulky Arginine side chain. Consistent with this possibility SiriusGFP has a pKa of 5.29 that also implies a proton repulsion effect of S147R near the phenolic group of the chromophore (Fig. S1D).

The UV-VIS spectroscopy of purified FPs revealed that SiriusGFP has a major excitation peak at 504 nm and a minor peak at 396 nm (Fig. 1A), indicating that the chromophore has two protonation states of the phenolic group, and that the protonated state is responsible for the minor peak. The extinction coefficient of SiriusGFP and eGFP are not significantly different (56,600 M^{-1} cm^{-1} at 504 nm for SiriusGFP, compared to 55,000 M^{-1} cm^{-1} at 488 nm for eGFP). The emission peak of SiriusGFP is at 516 nm (with a shoulder at ˜550 nm) instead of 508 nm for eGFP (with a shoulder at ˜540 nm). When excited at 400 nm SiriusGFP has the same emission peak at 516 nm (Fig. S1E), implying that ESPT occurs in SiriusGFP. Since the main proton pathway via Ser205 to Glu222 for ESPT was blocked by the mutation of S205 V, the alternative pathway via T203 is probably involved in ESPT of SiriusGFP. A proportion of Glu222 in SiriusGFP should be in the anionic state as a proton acceptor, while the majority of molecules maintains its chromophore in an anionic state along with a neutral Glu222. The ratio between the absorption intensities of the bands A:I in SiriusGFP (peak at 396 and 504 nm, respectively) is 1:3.75, whereas this ratio is 4 : 1 in wtGFP (peak at 400 nm and 488 nm). The fluorescence quantum yield (φ_f) of SiriusGFP is significantly reduced compared to eGFP (0.214 for SiriusGFP and 0.60 for eGFP) (Fig. S1C). Thus, the brightness (extinction coefficient X quantum yield) of SiriusGFP is 12,112 M^{-1} cm^{-1}, while eGFP is 33,000 M^{-1} cm^{-1}. These results imply that there are more competing pathways for deactivation of the excited state of SiriusGFP than that of eGFP. The decreased φ_f could be attributed to the increased τ-torsion on the chromophore by an absence of a constrained H-bond between Ser205 and the phenolic group of p-HBDI, which makes the phenolic group in SiriusGFP more flexible than that in eGFP. The τ-torsion (less than 90°) on the methylene bridge (the only exocyclic double bond) facilitates internal conversion and deactivation to ground state (Huang, Cheng et al. 2013) that can compete with the radiative relaxation as fluorescence.

The excitation and emission peak are both red-shifted from eGFP (Ex 488 nm, Em 508 nm) to SiriusGFP (Ex 504 nm, Em 516 nm), implying that the energy gap in SiriusGFP is narrower than that of eGFP and has more vibration levels in the S_0 and S_1 state.

When photobleaching transfected Hela cells with a scanning laser at 489 nm (~1500 μW at the objective) in a confocal microscope, exponential decay curves with different lifetimes (Tau) and residue offsets Y_0 were noted, and shown in Fig. 1B. The average lifetime (Tau) of SiriusGFP (118.3 s) is more than twice that of eGFP (50.1 s), with the intermediate mutants having values that lay between (Tau of SG205 is 104.4 s and SG147 is 76.3 s (Fig. 1C)). An ANOVA analysis on fluorescence lifetimes (Tau) among the four GFP variants indicates highly significant differences ($p < 0.01$). Thereafter, using Tukey-Kramer Multiple Comparisons Test for Tau pairwise comparison, Q values were 23.4 for eGFP and SiriusGFP, 19.2 for eGFP and SG205, 8.6 for eGFP and SG147, 5.1 for SiriusGFP and SG205, 13.7 for SiriusGFP and SG147, and 9.3 for SG205 and SG147. Note that a Q value of 3.6 or greater denotes a significant difference. Y_0 is the offset value with single exponential decay fitting, and represents the residual steady state fluorescence after photobleaching. Y_0 for SiriusGFP is 15.1% and is three fold that of eGFP (5.1%). Similar to Tau, the intermediate mutants had values that lay between that of eGFP and SiriusGFP (7.2% for SG205 and 12.5% for SG147 (Fig. 1C, D)). An ANOVA analysis on Y_0 among the four GFP variants also indicates significant differences ($p < 0.01$). As with Tau, these intermediate values resulted in a smaller degree of confidence in statistical differences of Y_0 between the SiriusGFP and the intermediate mutants when compared to SiriusGFP and eGFP. The Q values for Y_0 pairwise comparison were 36.7 for eGFP and SiriusGFP, 8.2 for eGFP and SG205, 27.6 for eGFP and SG147, 27.8 for SiriusGFP and SG205, 8.9 for SiriusGFP and SG147, 18.9 for SG205 and SG147. These data suggest that mutation of S205 V and S147R both contribute to the increase of Tau and Y_0. The combination of S205 V and S147R makes SiriusGFP superior to eGFP, although with a tradeoff in φ_f.

To compare brightness and photostability with the same amount of eGFP and SiriusGFP, the normalized photobleaching curves showed that the two variants have different rates of decay, and intersect at 167 s under constant laser power (~1500 μW) (Fig. 1E). The integrated area under curves are 423 for eGFP and 437 for SiriusGFP. The residual fluorescence of SiriusGFP is near four-fold higher than that of eGFP at the end of the long tail. With greater light intensity, the decay curves intersect at a shorter time point. Thus, for experiments requiring high intensity light SiriusGFP offers significantly greater advantages when longer exposures are required. These data also indicate that SiriusGFP emits more photons during long exposures or under high power illumination, although less than eGFP at the onset of exposure. In fact, at a given light intensity, the longer the exposure time the greater the differential advantage in photons emitted by SiriusGFP.

We also measured the photobleaching rates of GFPs with purified proteins embedded in polyacrylamide gel by laser-scanning confocal microscopy (Fig. 1F). This log-log plot of photobleaching rates versus illumination power showed nearly linear relationships that indicates an accelerated photobleaching of eGFP and SiriusGFP (Cranfill, Sell et al. 2016). The decay slope of SiriusGFP is similar to that of eGFP, but the lifetime is almost doubled. The photobleaching results measured with purified FPs in gel are similar to that in transfected cells.

Due to the long fluorescence tail of SiriusGFP, normal 3D confocal microscopy or superresolution microscopy, such as SIM, imaging quality can benefit.

3.2. Oxygen-depletion photobleaching

To explore the mechanisms of photobleaching in SiriusGFP we carried out photobleaching experiments with confocal microscopy under conditions of oxygen depletion. HELA cells separately transfected with eGFP-Omp25 and SiriusGFP-Omp25 were fixed in 4% PFA followed by oxygen-depletion treatment. Omp25 is a mitochondrial outer membrane protein, localized to the mitochondrial outer membrane anchoring by a single transmembrane segment at the C-terminal. Overexpression of OMP25 results in perinuclear clustering of mitochondria in transfected cells (Nemoto and De Camilli, 1999). eGFP and SiriusGFP were fused on the N terminus of Omp25. Photobleaching of eGFP and SiriusGFP was performed under aerobic and anaerobic conditions at low and high laser power. When photobleaching with low laser power (˜150 μW) both eGFP and Sirius GFP show sensitivity to oxygen. In contrast, at high laser power (˜1500 μW) photobleaching of eGFP is not oxygen dependent, while SiriusGFP shows oxygen-dependence (Fig. 2). In all these conditions SiriusGFP remained more photostable than eGFP. It is believed that GFP's differential sensitivity to oxygen under differing intensities of light points to different mechanisms of photobleaching (Tsien, 1998; Greenbaum, Rothmann et al. 2000; Jimenez-Banzo, Nonell et al. 2008; Grigorenko, Nemukhin et al. 2015). High photon flux may lead to higher-order photobleaching due to a multi-photon effect (Chen, Zeng et al. 2002). Our data indicate that the photobleaching mechanisms of SiriusGFP are different from that in eGFP, particularly in high intensity light. We infer that SiriusGFP is resistant to high-order photobleaching in high intensity light.

3.3. Practical applications 1. 4D confocal scanning

To test the performance of SiriusGFP in confocal microscopy, we carried out an experiment with 4D confocal imaging on live HeLa cells. Cells were transfected with eGFP-Omp25 and SiriusGFP-Omp25 and imaged live in PBS (Fig. 3). In this experiment, 3D confocal Z-stack scanning was done in continuous mode to maximize photobleaching. The 4D confocal imaging results indicate a dramatic improvement of image clarity due to the photostability of SiriusGFP (more than 30 min) compared to eGFP (˜10 min). Indeed, after longer exposure (60 min) under the same conditions, SiriusGFP-Omp25 cells continued to exhibit vivid images of intracellular mitochondria (Fig. S3). For instance, the outline of mitochondria were not visible after 60 min of continuous imaging of OMP25 eGFP, but were clearly visible with Sirius GFP.

3.4. Practical applications 2. Structured illumination microscopy (SIM)

We sought to ascertain if SiriusGFP improved the quality of superresolution microscopy, where the demands on photostability are pronounced. We used structured illumination microscopy (SIM) to explore the advantages of SiriusGFP. The SIM images of fixed HEK-293 cells expressing SiriusGFP-Omp25 was compared to eGFP-Omp25. The image resolution of SIM with SiriusGFP was significantly improved (Fig. 4).

Quantitative measures in Z planes, in particular, show marked improvement in image quality. We repeated the SIM imaging of fixed Hela cells expressing SiriusGFP-Omp25 and eGFP-Omp25, respectively. Peak to peak Gaussian fitting of over 100 peaks showed an XY resolution of SiriusGFP-Omp25 to be 130 ± 1.4 nm, similar to eGFP-OMP25

with an XY resolution of 131 ± 1.8 nm (p = 0.546). In contrast, the Z axis resolution of SiriusGFP-Omp25 was 310 ± 4.6 nm and significantly improved (p = 0.0017) over that of eGFP-Omp25 at 335 ± 5.6 nm. These values of SiriusGFP are approaching the limit of SIM resolution (Gustafsson, 2000; Heintzmann and Huser, 2017). Both total photon number and point of spread function (PSF) are key determinants of image quality and resolution. The increased resolution in the Z axis indicates that more photons were collected by the photoelectronic detector with SiriusGFP-Omp25 compared to eGFP-Omp25 since the PSF should be similar.

Although the XY resolution is similar by analysis of profile peaks after the Gaussian fitting of SIM, absent in the quantitative assessment were the qualitative differences in these two FPs. The majority of mitochondria using eGFP-OMP25 demonstrated absent membrane segments on the Z reconstructions (top and bottom profiles) while those using SiriusGFP-OMP25 were much more integrated (Fig. 4). In the XY plane, the mitochondrial membrane labeled with SiriusGFP-OMP25 showed very clear and detailed images; for instance, fission-fusion processes and twisted structures under stress. In contrast, many parts of the mitochondrial membrane labeled with eGFP-OMP25 showed broken/ discontinuous profiles that are likely artifacts from photobleaching (Fig. 5) (Figure.S4). The slower photobleaching of SiriusGFP made superresolution imaging better with more detailed information of subcellular organelles, and also produced less imaging artifacts than eGFP.

4. Discussion

We have developed an improved version of eGFP, named SiriusGFP, that shows a more than 2-fold increase in photostability compared to eGFP and is able to fold well with both N and C terminal fusion proteins. Prestin-SiriusGFP with SiriusGFP fused to the C-terminus of prestin, and SiriusGFP-OMP25 with SiriusGFP fused to the N-terminus of Omp25 both fold well. We have confirmed the obvious biological applicability of SiriusGFP using SIM and 4D confocal microscopy, and explored photobleaching mechanisms for SiriusGFP and eGFP. A number of points about the mechanism of photostability bear discussion below.

In GFPs, there is a seesaw-like action on protonation between the chromophore (*p*-HBDI) and Glu222. In wtGFP, the chromophore is mainly protonated (80% in neutral state), while Glu222 is correspondingly in a deprotonated anion state. This proton movement is brought about by excited state proton transfer (ESPT). In contrast, the chromophore of eGFP is deprotonated (anion state) while Glu222 is protonated (neutral) at physiological pH (Bettati, Pasqualetto et al. 2011). In SiriusGFP, the chromophore is mixed with the major deprotonated (anion state) and the minor protonated form at a ratio of 4:1 (80% in anion state), and the same emission peak can be observed when excited at ˜398 nm, indicating ESPT exists in SiriusGFP. But the minor protonated population that absorbs at 396 nm may not be the reason why SiriusGFP is more photostable than eGFP because wtGFP has larger absorption peak at 400 nm, while it is less photostable than eGFP.

Photobleaching in GFPs induced by UV/visible light or X-ray was determined to be related to Glu222 decarboxylation as a point of primary damage and the consequent rearrangement of the H-bond network (van Thor et al., 2002; Bell, Stoner-Ma et al. 2003; Royant and

Noirclerc-Savoye, 2011; Arpino, Rizkallah et al. 2012). Glu222 contributes to the rigidity of the chromophore cavity by H-bonding adjacent residues and a cluster of water molecules. The decarboxylation of Glu222 results in the collapse of the H-bonding network next to the chromophore, and further promotes non-irradiative relaxation to the ground state or chromophore destruction (Royant and Noirclerc-Savoye, 2011). Still, there is a gap in our understanding of Glu222 decarboxylation and final chromophore destruction.

Light or X-ray irradiation on FPs can produce radical species by electron transfer (ET) from the excited chromophore. It was suggested that in wtGFP and PA-GFP the excitation of chromophore may promote charge transfer from Glu222 to the chromophore. This induces a biradical state that then relaxes back to the ground state or occasionally leads to decarboxylation of Glu222 that, in turn, leads to permanent chromophore destruction (Adam, Carpentier et al. 2009). The Kolbe mechanism was proposed to be responsible for the photoinduced decarboxylation of Glu222 in wtGFP (van Thor et al., 2002). However, after ultrafast ESPT in femtosecond scale the excited chromophore is turned to an anionic state that may not be able to be an electron acceptor. Moreover, in eGFP the chromophore is dominantly in the anion state. Another photophysical pathway had been proposed that triggers redox reactions inside GFP (Bochenkova, Klaerke et al. 2014), in which the chromophore anion $HBDI^-$ undergoes an photodetachment upon absorption of one-photon UV or multi-photon visible light to produce a solvated electron and a radical chromophore. Thereafter, the photo-oxidized radical chromophore can accept an electron as an oxidant in Glu222 decarboxylation.

The interruption of the proton wire between HBDI and Glu222 by S205 V may hinder the electron transfer, therefore reducing the possibility of the biradical state and further chromophore destruction. However, the double mutant of eGFP-T203 V/S205 V that lacks both possible pathways of ESPT also shows photobleaching (data not shown), implying that the photobleaching pathway may not be limited by Glu222 damage.

4.1. Z-E isomerization

Upon excitation of chromophore *p*-HBDI of GFPs, the *Z-E* isomerization undergoes the τ-torsion around the only exocyclic double bond with a τ angle smaller than 90°, followed by internal conversion (IC) mostly to the ground state of Z isomers. The τ-torsion transiently disrupts the conjugated π-electron system for reversible loss in fluorescence, which could be the major non-radiative decay channel for the excited state S_1 of *p*-HBDI in GFPs (Chatterjee, Mandal et al. 2015).

In eGFP, the first excited state S_1 deactivates mainly via fluorescence with high quantum yield (˜0.60) attributed to limiting τ-rotation around the only exocyclic double bond by H-bond network.

That the quantum yield φ_f of SiriusGFP is smaller than that of eGFP is probably due to less constraints on the phenolic group of *p*-HBDI; the lack of H-bond binding on Ser205 facilitates τ-torsion and thereby could increase internal conversion by facilitating τ-torsion along the methylene bridge between imidazolinone and phenolate moieties. Meanwhile, the τ-torsion with less constraints in SiriusGFP may also increase the possibility of internal

conversion from S_n to S_{n-1} (e.g., $S_1 \longleftarrow S_2$ or $S_2 \longleftarrow S_3$). This in turn can decrease the possibility of electron-detachment and subsequent chromophore destruction. Quantum yield is proportional to brightness, but may not directly affect photostability. That is, lower quantum yield does not mean higher photostability. For instance, most red FPs have low quantum yield (< 0.20) but are still easily photobleached (Cranfill, Sell et al. 2016). The electron transfer during deactivation may be the critical step for chromophore damage.

The methylene bridge between imidazolinone and phenolate moieties can perform τ-torsion for internal conversion or lead to Glu222 decarboxylation and chromophore destruction, depending on how many photons are absorbed by the chromophore and if ROS or solvated electrons nearby are available. A nearby oxygen can accept a photoelectron from the anionic GFP chromophore to form superoxide radicals on the exocyclic methylene bridge of the chromophore. This superoxide radical consequently undergoes a further series of chemical reactions resulting in the cleavage of the exocyclic bridging bond of the chromophore resulting in permanent bleaching (Grigorenko, Nemukhin et al. 2015). The electron transfer in eGFP may occur from the chromophore anion to external oxidants via an intermediate aromatic residue, Tyr145 (Bogdanov, Acharya et al. 2016). Substitution of key residues controlling electron transfer to external oxidants would be expected to increase photostability, although the detailed effects on different substituted residues need further investigation (Hosoi, Hazama et al. 2015). We tested mutation of Y145 l and Y145E in eGFP and SiriusGFP. Both mutants showed dimmed fluorescence (data not shown), perhaps due to the over 3-fold decrease in the extinction coefficients of Y145 l or Y145E (Bogdanov, Acharya et al. 2016). S147R associating with H148 at the entrance of access to the phenolic group of the chromophore may help block exterior ROS. Both its positive charge and bulky side chain could contribute to the photostability without the fast decay phase seen in N149 K in Emerald-GFP. The photobleaching results (Fig. 1B) suggest that S147R may play an important role in blocking the entrance of external oxidants or, alternatively, affecting the electron transfer efficiency to external oxidants.

In summary, photobleaching is one of the major problems for genetically encoded FPs, which limits their application in biological investigations. We have developed a FP, SiriusGFP, that shows significant improvement in photostability over eGFP in high and low intensity illumination. While Sirius GFP has reduced brightness compared to eGFP, its 2-fold increase in photostability allows for much improved imaging requiring high or prolonged intensity light. In practical terms this gain in stability allows imaging without a dynamic adjustment in exposure time and light intensity with increasing experimental time. Our new FP will provide improved capabilities for superresolution and time-dependent confocal microscopy.

Supplementary Material

Refer to Web version on PubMed Central for supplementary material.

Acknowledgement

We would like to thank Dr. Lena Schroeder for kindly sharing eGFP-Omp25 plasmid with us.

This work was funded by the National Institute of Health grant, NIDCD R01 DC 000273 and NIDCD R01 DC 016318 to J.S.S., R01 DC 008130 to J.S.S. and D.S.N., and R01 DC 007894 to D.S.N.

References

Adam V, Carpentier P, Violot S, Lelimousin M, Darnault C, Nienhaus GU, Bourgeois D, 2009. Structural basis of X-ray-induced transient photobleaching in a photoactivatable green fluorescent protein. J. Am. Chem. Soc 131 (50), 18063–18065. [PubMed: 19950947]

Andrews BT, Schoenfish AR, Roy M, Waldo G, Jennings PA, 2007. The rough energy landscape of superfolder GFP is linked to the chromophore. J. Mol. Biol 373 (2), 476–490. [PubMed: 17822714]

Arpino JA, Rizkallah PJ, Jones DD, 2012. Crystal structure of enhanced green fluorescent protein to 1.35 A resolution reveals alternative conformations for Glu222. PLoS One 7 (10) e47132.

Baker BJ, Mutoh H, Dimitrov D, Akemann W, Perron A, Iwamoto Y, Jin L, Cohen LB, Isacoff EY, Pieribone VA, Hughes T, Knopfel T, 2008. Genetically encoded fluorescent sensors of membrane potential. Brain Cell Biol. 36 (1–4), 53–67. [PubMed: 18679801]

Bell AF, Stoner-Ma D, Wachter RM, Tonge PJ, 2003. Light-driven decarboxylation of wild-type green fluorescent protein. J. Am. Chem. Soc 125 (23), 6919–6926. [PubMed: 12783544]

Bettati S, Pasqualetto E, Lolli G, Campanini B, Battistutta R, 2011. Structure and single crystal spectroscopy of Green Fluorescent Proteins. Biochim. Biophys. Acta 1814 (6), 824–833. [PubMed: 20940063]

Bochenkova AV, Klaerke B, Rahbek DB, Rajput J, Toker Y, Andersen LH, 2014. UV excited-state photoresponse of biochromophore negative ions. Angew. Chem. Int. Ed. Engl 53 (37), 9797–9801. [PubMed: 25044707]

Bogdanov AM, Bogdanova EA, Chudakov DM, Gorodnicheva TV, Lukyanov S, Lukyanov KA, 2009. Cell culture medium affects GFP photostability: a solution. Nat. Methods 6 (12), 859–860. [PubMed: 19935837]

Bogdanov AM, Acharya A, Titelmayer AV, Mamontova AV, Bravaya KB, Kolomeisky AB, Lukyanov KA, Krylov AI, 2016. Turning On and Off Photoinduced Electron Transfer in Fluorescent Proteins by pi-Stacking, Halide Binding, and Tyr145 Mutations. J. Am. Chem. Soc 138 (14), 4807–4817. [PubMed: 26999576]

Chatterjee T, Mandal M, Gude V, Bag PP, Mandal PK, 2015. Strong electron donation induced differential nonradiative decay pathways for para and meta GFP chromophore analogues. Phys. Chem. Chem. Phys 17 (32), 20515–20521. [PubMed: 26176350]

Chen TS, Zeng SQ, Luo QM, Zhang ZH, Zhou W, 2002. High-order photobleaching of green fluorescent protein inside live cells in two-photon excitation microscopy. Biochem. Biophys. Res. Commun 291 (5), 1272–1275. [PubMed: 11883955]

Chen TW, Wardill TJ, Sun Y, Pulver SR, Renninger SL, Baohan A, Schreiter ER, Kerr RA, Orger MB, Jayaraman V, Looger LL, Svoboda K, Kim DS, 2013. Ultrasensitive fluorescent proteins for imaging neuronal activity. Nature 499 (7458), 295–300. [PubMed: 23868258]

Cranfill PJ, Sell BR, Baird MA, Allen JR, Lavagnino Z, de Gruiter HM, Kremers GJ, Davidson MW, Ustione A, Piston DW, 2016. Quantitative assessment of fluorescent proteins. Nat. Methods 13 (7), 557–562. 10.1038/nmeth.3891. Epub 2016 May 30. PMID: . [PubMed: 27240257]

Cubitt AB, Woollenweber LA, Heim R, 1999. Understanding structure-function relationships in the Aequorea victoria green fluorescent protein. Methods Cell Biol. 58, 19–30. [PubMed: 9891372]

Erez Y, Gepshtein R, Presiado I, Trujillo K, Kallio K, Remington SJ, Huppert D, 2011. Structure and excited-state proton transfer in the GFP S205A mutant. J. Phys. Chem. B 115 (41), 11776–11785. [PubMed: 21902228]

Fang C, Frontiera RR, Tran R, Mathies RA, 2009. Mapping GFP structure evolution during proton transfer with femtosecond Raman spectroscopy. Nature 462 (7270), 200–204. [PubMed: 19907490]

Fukuda H, Arai M, Kuwajima K, 2000. Folding of green fluorescent protein and the cycle3 mutant. Biochemistry 39 (39), 12025–12032. [PubMed: 11009617]

Greenbaum L, Rothmann C, Lavie R, Malik Z, 2000. Green fluorescent protein photobleaching: a model for protein damage by endogenous and exogenous singlet oxygen. Biol. Chem 381 (12), 1251–1258. [PubMed: 11209760]

Grigorenko BL, Nemukhin AV, Polyakov IV, Khrenova MG, Krylov AI, 2015. A Light-Induced Reaction with Oxygen Leads to Chromophore Decomposition and Irreversible Photobleaching in GFP-Type Proteins. J. Phys. Chem. B 119 (17), 5444–5452. [PubMed: 25867185]

Gustafsson MG, 2000. Surpassing the lateral resolution limit by a factor of two using structured illumination microscopy. J. Microsc 198 (Pt 2), 82–87. [PubMed: 10810003]

Heintzmann R, Huser T, 2017. Super-resolution structured illumination microscopy. Chem. Rev 117 (23), 13890–13908. [PubMed: 29125755]

Hong S, Wilton DK, Stevens B, Richardson DS, 2017. Structured illumination microscopy for the investigation of synaptic structure and function. Methods Mol. Biol 1538, 155–167. [PubMed: 27943190]

Hosoi H, Hazama S, Takeda Y, 2015. Smaller 145th residue makes fluorescent protein non-fluorescent: Fluorescence lifetimes of enhanced yellow fluorescent protein (eYFP) Y145 mutants and H148 mutants. Chem. Phys. Lett 618, 186–191.

Huang GJ, Cheng CW, Hsu HY, Prabhakar C, Lee YP, Diau EW, Yang JS, 2013. Effects of hydrogen bonding on internal conversion of GFP-like chromophores. I. The para-amino systems. J. Phys. Chem. B 117 (9), 2695–2704. [PubMed: 23347151]

Jimenez-Banzo A, Nonell S, Hofkens J, Flors C, 2008. Singlet oxygen photosensitization by EGFP and its chromophore HBDI. Biophys. J 94 (1), 168–172. [PubMed: 17766345]

Nemoto Y, De Camilli P, 1999. Recruitment of an alternatively spliced form of synaptojanin 2 to mitochondria by the interaction with the PDZ domain of a mitochondrial outer membrane protein. EMBO J. 18 (11), 2991–3006. [PubMed: 10357812]

Nielsen SB, Lapierre A, Andersen JU, Pedersen UV, Tomita S, Andersen LH, 2001. Absorption spectrum of the green fluorescent protein chromophore anion in vacuo. Phys. Rev. Lett 87 (22) 228102.

Niwa H, Inouye S, Hirano T, Matsuno T, Kojima S, Kubota M, Ohashi M, Tsuji FI, 1996. Chemical nature of the light emitter of the Aequorea green fluorescent protein. Proc. Natl. Acad. Sci. U. S. A 93 (24), 13617–13622. [PubMed: 8942983]

Olivier N, Keller D, Gonczy P, Manley S, 2013. Resolution doubling in 3D-STORM imaging through improved buffers. PLoS One 8 (7).

Ottmann C, Weyand M, Wolf A, Kuhlmann J, Ottmann C, 2009. Applicability of superfolder YFP bimolecular fluorescence complementation in vitro. Biol. Chem 390 (1), 81–90. [PubMed: 19007309]

Pedelacq JD, Cabantous S, Tran T, Terwilliger TC, Waldo GS, 2006. Engineering and characterization of a superfolder green fluorescent protein. Nat. Biotechnol 24 (1), 79–88. [PubMed: 16369541]

Rego EH, Shao L, 2015. Practical structured illumination microscopy. Methods Mol. Biol 1251, 175–192.

Royant A, Noirclerc-Savoye M, 2011. Stabilizing role of glutamic acid 222 in the structure of enhanced Green Fluorescent Protein. J. Struct. Biol 174 (2), 385–390. [PubMed: 21335090]

Shu X, Leiderman P, Gepshtein R, Smith NR, Kallio K, Huppert D, Remington SJ, 2007. An alternative excited-state proton transfer pathway in green fluorescent protein variant S205V. Protein Sci. 16 (12), 2703–2710. [PubMed: 17965188]

Tsien RY, 1998. The green fluorescent protein. Annu. Rev. Biochem 67, 509–544. [PubMed: 9759496]

van Thor JJ, Gensch T, Hellingwerf KJ, Johnson LN, 2002. Phototransformation of green fluorescent protein with UV and visible light leads to decarboxylation of glutamate 222. Nat. Struct. Biol 9 (1), 37–41. [PubMed: 11740505]

Wineman-Fisher V, Simkovitch R, Shomer S, Gepshtein R, Huppert D, Saif M, Kallio K, Remington SJ, Miller Y, 2014. Insight into the structure and the mechanism of the slow proton transfer in the GFP double mutant T203V/S205A. Phys. Chem. Chem. Phys 16 (23), 11196–11208. [PubMed: 24776960]

Yang JS, Huang GJ, Liu YH, Peng SM, 2008. Photoisomerization of the green fluorescence protein chromophore and the meta- and para-amino analogues. Chem. Commun. (Camb.) (11), 1344–1346. [PubMed: 18389128]

Zacharias DA, Violin JD, Newton AC, Tsien RY, 2002. Partitioning of lipid-modified monomeric GFPs into membrane microdomains of live cells. Science 296 (5569), 913–916. [PubMed: 11988576]

Zhong S, Navaratnam D, Santos-Sacchi J, 2014. A genetically-encoded YFP sensor with enhanced chloride sensitivity, photostability and reduced ph interference demonstrates augmented transmembrane chloride movement by gerbil prestin (SLC26a5). PLoS One 9 (6) e99095.

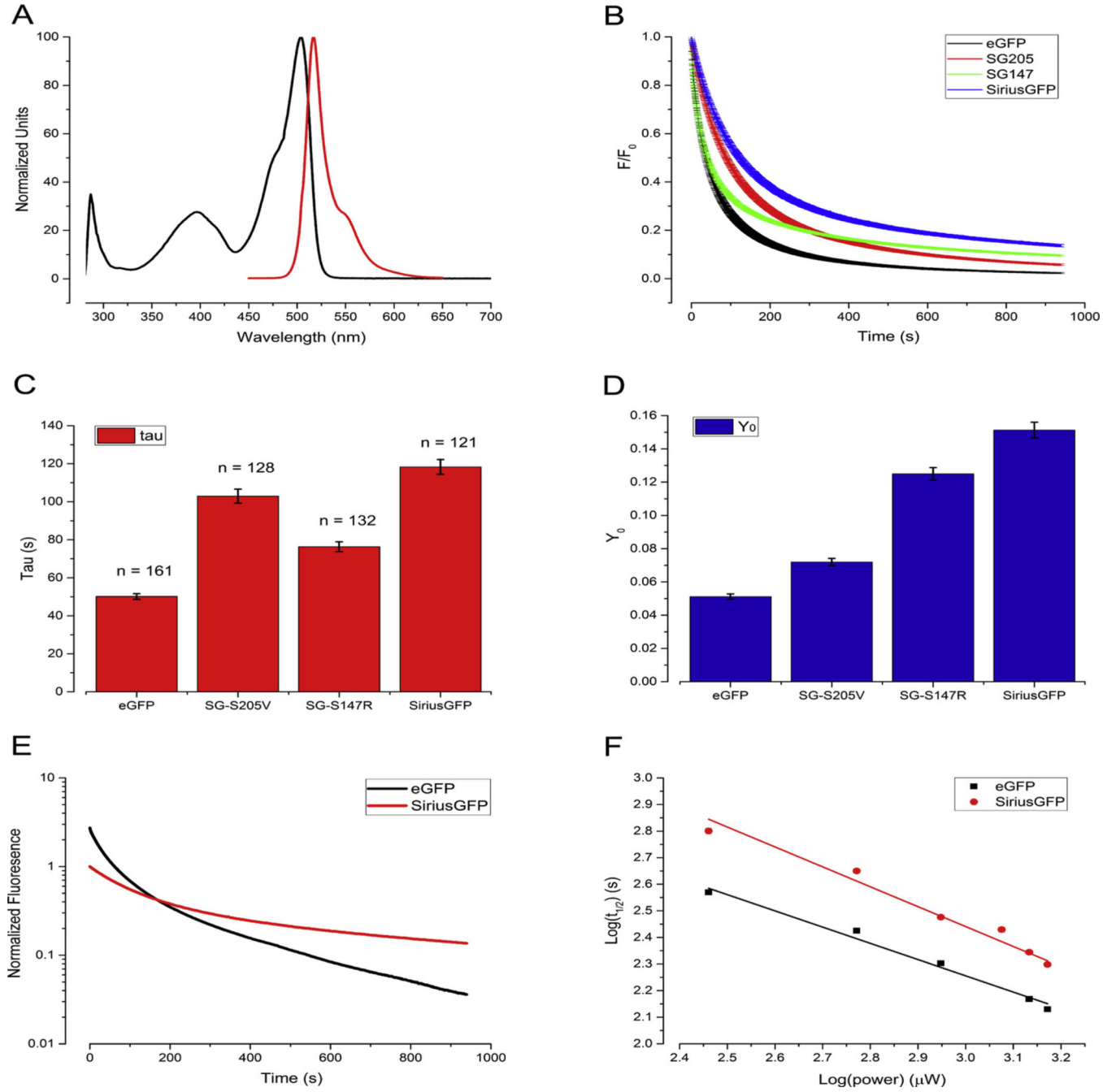

Fig. 1.

Optical properties of SiriusGFP compared to eGFP. **(A)** The UV–vis spectrum of SiriusGFP indicates that the protonate chromophore exists in a minor proportion. Shown is the UV–vis absorbance and fluorescent spectrum of purified SiriusGFP in a buffer of 150 mM NaCl, 20 mM Tris, pH7.5. SiriusGFP has a major excitation peak at 504 nm and a minor peak at 396 nm, implying that the protonated chromophore exists in minor proportion. **(B)** SiriusGFP is more photostable than eGFP. Shown are the photobleaching curves of eGFP, SG205, SG147, and SiriusGFP expressed in Hela cells. Fluorescence was detected by laser

irradiation of live cells at 489 nm on a Zeiss confocal microscope (Zeiss LSM 710 duo). We determined that the photostability of SiriusGFP is > 2.4 fold higher than that of eGFP. The ratio of integrated areas under the curves is 1 : 1.99 : 1.88 : 3.34 for eGFP : SG205 : SG147 : SiriusGFP. The optical power of scanning laser at 489 nm was ˜1500 μW. Each curve is the average of > 100 cells with standard error accounting for the variability in the thickness of each line. **(C)** SiriusGFP shows increased photobleaching time constants compared to eGFP. Photobleaching data can be fit by a single exponential decay function, $Y = Y_0 + Ae^{-x/t}$, where Y_0 is the constant offset representing the residual fluorescence after photobleaching reached a steady state (R^2 ranged from 0.97–0.99). The single exponential fitting on photobleaching curves determined that the lifetime (Tau) of SiriusGFP is 118.3 s, 102.9 s for SG205, 76.3 s for SG147, compare to 50.1 s for eGFP under the same photobleaching conditions. The cell numbers (n) are shown on the top of each sample. The error bar is standard error. ANOVA analysis of Tau values shows high confidence in statistically significant differences (p-value 2.42×10^{-50}). **(D)** Residual fluorescence in SiriusGFP is greater than eGFP after prolonged photobleaching. Y_0 represents the residual fluorescence after photobleaching; 15.1% for SiriusGFP compared to 12.5% for SG147, 7.2% for SG205 and 5.1% of eGFP. The error bar is standard error. **(E)** The choice of eGFP and SiriusGFP depends on the intended duration of an experiment. The normalized photobleaching curves with the same amount of eGFP and SiriusGFP show the two curves crossing at 167 s. At the end of long tail, the residual fluorescence of SiriusGFP is 3.76-fold higher than that of eGFP. The integrated area is 423.4 for eGFP, and 437.6 for SiriusGFP, confirming that SiriusGFP emits more photons upon prolonged exposure. Conversely, the number of photons emitted in short durations is greater in eGFP, which is therefore preferred in experiments with short fluorescence emission. **(F)** Across a range of light intensities SiriusGFP maintains its superior photobleaching characteristics compared to eGFP. Shown is a log-log plot of photobleaching rates versus illumination laser power of the laser-scanning confocal microscope using purified SiriusGFP and eGFP embedded in polyacrylamide (see method section). SiriusGFP shows slower rates of photobleaching at different light intensities compared to eGFP. Data were fitted to the equation $\log(F) = -\alpha\log(P) + c$, where F is the photobleaching half-time constant and P is the illumination power, α is 0.61 for eGFP and 0.75 for SiriusGFP, while c is 4.1 for eGFP and 4.7 for SiriusGFP.

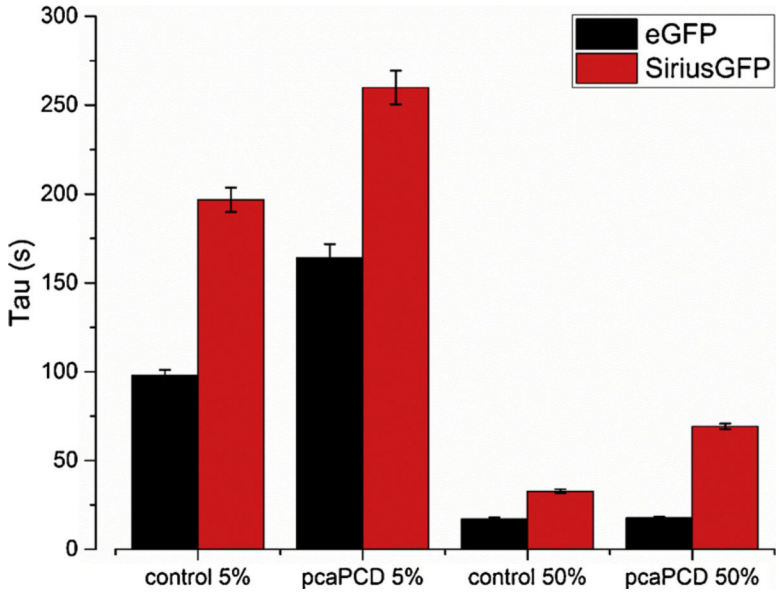

Fig. 2.

Photobleaching of SiriusGFP-Omp25 is oxygen dependent across a range of light intensities and contrasts with eGFP-Omp25. Shown are the photobleaching time constants of eGFP and SiriusGFP in PFA-fixed Hela cells with (pcaPCD – see section 7 in Methods) and without (control) oxygen-depletion solution under low and high optical power illumination, respectively. The percentage of laser power (5% and 50%) at 489 nm used for photobleaching corresponded to measured light intensities of 150 μW (5%) and 1500 μW (50%) at the objective. The error bar is standard error. At high and low intensity light, photobleaching of SiriusGFP is oxygen dependent. In contrast, eGFP is oxygen dependent only in low intensity light.

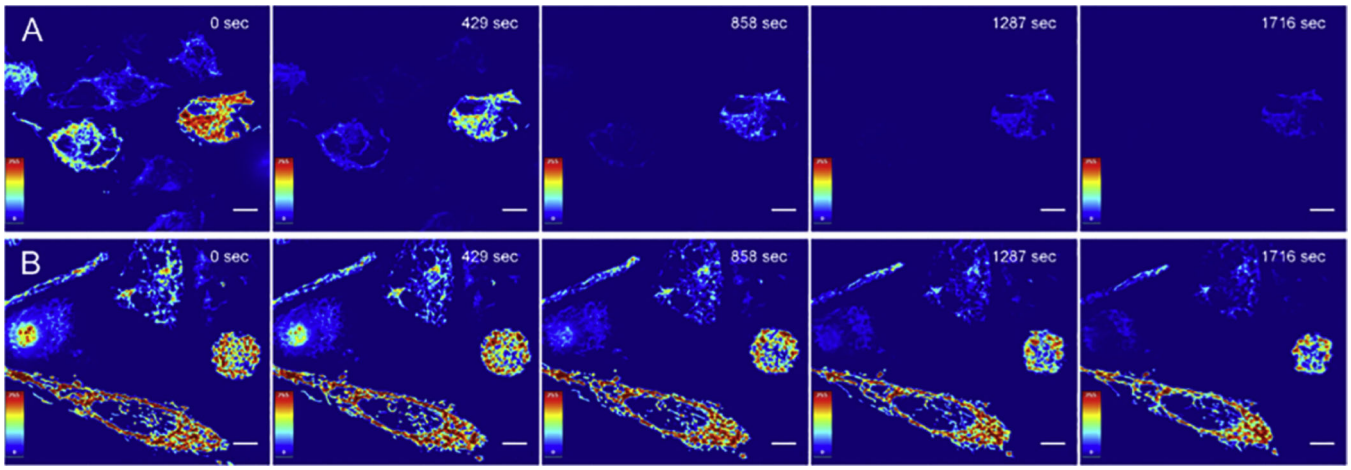

Fig. 3.

Continuous confocal 4D imaging of live HeLa cells, in PBS, transfected with eGFP-Omp25 (**A**, upper panel) and SiriusGFP-Omp25 (**B**, lower panel), respectively. The confocal Z-stack scanning was continuous, and lasted 30 min. The color table for intensity is shown in the images. The data show SiriusGFP to be significantly resistant to photobleaching with markedly improved image quality even at 30 min. In contrast eGFP shows rapid degradation of image quality owing to photobleaching even at 7 min (429 s). The sale bar is 15 μm.

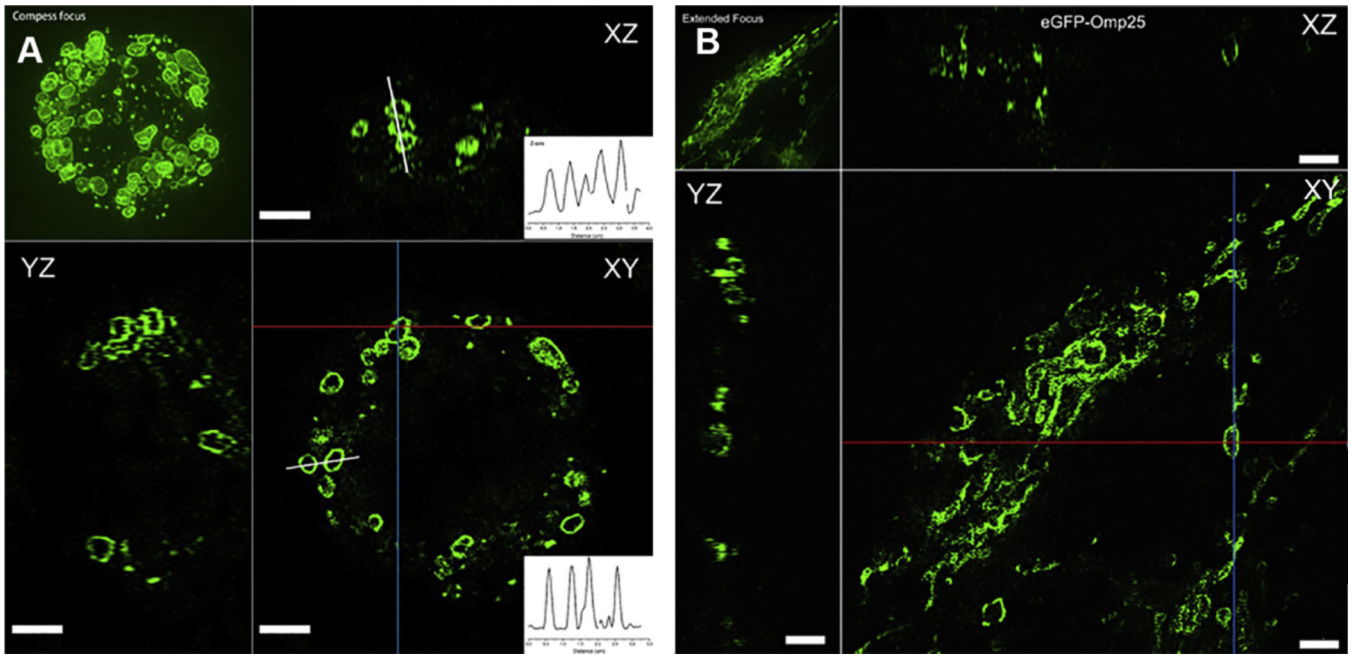

Fig. 4.

SiriusGFP enhances SIM image quality, particularly in the Z axis. **(A)** Shown is the XYZ profile of SiriusGFP-Omp25 transfected HEK-293 cells captured by Structured Illumination Microscopy (SIM, DeltaVision-OMX, Applied Precision, GE life). The blue and red lines indicate the locations where the YZ (upper panel) and XZ (left panel) profiles were obtained. One can distinguish individual mitochondria even from Z axis images. The same image with extended focus has been attached to the left-upper corner. Two line measurements (white line) were performed on individual mitochondria in the Z and XY axes (right inset), respectively. We then used Gaussian fitting of the readout traces to obtain estimates of full width at half maximum (FWHM). **(B)** Shown is the XYZ profile of eGFP-Omp25. Many of Z profile of mitochondrial outer membrane were missing, and even some of XY profile also showed many discontinuous lines. The scale bar in A is 2.5 μm and B is 2.2 μm.

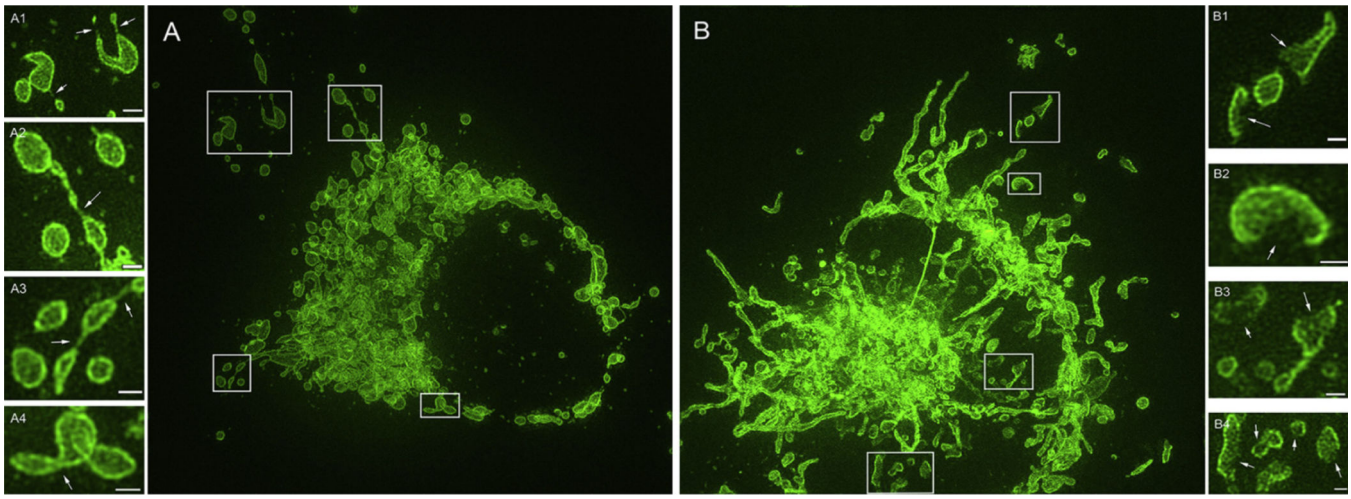

Fig. 5.

(A) SiriusGFP shows qualitative enhancement in SIM images in the XY plane. A SIM image of SiriusGFP-Omp25 in Hela cells. This sample was fixed with 4% PFA and imaged in PBS. The insets are the enlarged area of the white boxes. The uniformity of the mitochondrial outer membrane and the z-axis accumulation was very well achieved. A number of details can be discerned in the high quality images including mitochondrial fusion/fission (A1–3, arrows) and bended/twisted (A-4, arrows) structures shown in the insets.

(B) In the XY plane of eGFP is qualitatively inferior to SiriusGFP in SIM imaging. A SIM image of eGFP-Omp25 in Hela cells. This sample was fixed with 4% PFA and imaged in PBS. The insets are the enlarged area of the white boxes. The uniformity of the mitochondrial outer membrane was interrupted by obvious breaks (B1–4, arrows) and the Z-axis accumulation cannot be well achieved due to the photobleaching of eGFP. The patchy depletion of the mitochondrial outer membranes are notable (B, B1–4). These images are in contrast to those obtained with SiriusGFP, where mitochondrial outer membranes show consistent and uniform patterns with no artifactual loss (A, A1–4). The scale bars are 0.5 μm.